

Programmable Gilbert Damping in Py/Cu/Fe-Co-Tb Structures with Dynamic Interlayer Coupling


Qian Chen^{1,2,§}, Qingjie Guo,^{1,§} Wen Zhang,³ Ping Kwan Johnny Wong^{3,†}, Zhaocong Huang,¹ Zhaoxia Kou,¹ Jun Du,⁴ Zhongming Zeng,^{2,†} and Ya Zhai^{1,*}

¹*School of Physics, Southeast University, Nanjing 211189, China*

²*Nanofabrication facility, Suzhou Institute of Nano-Tech and Nano-Bionics, Chinese Academy of Sciences, Suzhou, Jiangsu 215123, China*

³*School of Microelectronics, Northwestern Polytechnical University, Xi'an 710072, China*

⁴*National Laboratory of Solid State Microstructures, Nanjing University, Nanjing 210093, China*

 (Received 23 September 2021; revised 22 December 2021; accepted 17 February 2022; published 9 March 2022)

Magnetodynamics of magnetic nanolayers is central to the emerging research field of magnonics. Here, we demonstrate an effective tuning of the dynamic properties of permalloy (Py, response layer) thin films, by capping with Cu/Fe-Co-Tb (spin-sink layer) layers with adjustable interlayer coupling and magnetic configurations. The strategy enables a remarkably enhanced Gilbert damping of the response layer, by about 10 times; this enhancement is higher than most of the results reported so far. More importantly, dynamic damping is programmable between the two opposite configurations (parallel vs antiparallel) in Py and Fe-Co-Tb and remains intact even in the form of nano- and microdevices. The interlayer coupling between Py and Fe-Co-Tb is systematically studied by changing the thickness of the Cu spacer. It is demonstrated that the dynamic interlayer coupling between ferromagnetic layers plays the key role in increased damping. Our work provides a feasible route towards reconfigurable magnonic devices, especially for logic and high-speed computing.

DOI: [10.1103/PhysRevApplied.17.034027](https://doi.org/10.1103/PhysRevApplied.17.034027)

I. INTRODUCTION

The field of magnonics, which aims to use spin waves as carriers of information, has provided a paradigm of computing technologies with low-power consumption [1–3]. In this context, the Gilbert-damping constant, α , becomes an important figure of merit, which determines the dynamic behavior of a given magnetic material [4]. Commonly, a large value of such a constant is expected to enable high-speed magnetization switching, while a small value benefits a reduced threshold current in devices operating with the spin-torque mechanism. In addition, a tunable Gilbert damping is desired to further control spin-wave propagation in a magnetic material, which acts as the transport medium of a magnonic device [5,6]. Therefore, Gilbert-damping control is significant for striking a balance between the operating speed and power consumption of reconfigurable magnonic devices.

To manipulate Gilbert damping, various experimental strategies are adopted, including impurity doping [7], electric field effect [8], spin-orbit torques [9], and spin pumping [10,11]. Among these methods, impurity doping is by far the most efficient. Our previous studies have, for instance, reported a remarkably enhanced Gilbert damping of permalloy ($\text{Ni}_{80}\text{Fe}_{20}$, Py) with dilute Tb doping [12]. However, the intrinsic soft magnetism of Py tends to be interrupted by foreign dopants. The associated change of α is also irreversible, thus failing to meet the requirements of magnonic logic devices.

The spin-pumping effect, on the other hand, allows engineering of the damping constant of a ferromagnetic film (FM) by an adjacent normal-metal (NM) film. When a pure spin current is generated from the precessing FM, it will be relaxed in the NM resulting from the spin-pumping effect. In this case, the Gilbert damping of the FM is enhanced, while other magnetic properties of the FM remain largely unaffected [10]. The efficiency of the spin-pumping effect is usually proportional to spin-orbit coupling (SOC) of the NM layer. This is an advantage for heavy metals, such as Pt, W, and Ta, the spin-flip relaxation time of which is short due to the large SOC, whereas, for light metals, such as Al and Cu, the Gilbert damping of the FM is hard to control due to the weak SOC. Therefore,

*yazhai@seu.edu.cn

†zmzeng2012@sinano.ac.cn

‡pingkwanj.wong@nwpu.edu.cn

§Q. Chen and Q. Guo contributed equally to this work.

additional relaxation channels for the pumped spin current are needed to control the Gilbert damping of the FM. Dynamic interlayer coupling is one such channel [13], relying on the interaction of spin currents pumped from the precessing magnetization of each magnetic layer in a spin-valve structure (FM1/NM/FM2) [14]. In this kind of structure, the FM2 layer acts as a sink for the transverse spin current, which gives rise to effective control of α of FM1, depending on the spin-valve configuration [15–17]. Despite the clear physical concept involved, effective tuning of α associated with this type of magnetic heterostructure remains largely unexplored, however.

Here, combining the advantages of spin pumping and impurity doping, this work demonstrates the effective tuning of Gilbert damping in Py. This strategy is achieved by adjustable interlayer coupling and magnetic configurations in Py/Cu/(Fe₅₀Co₅₀)_{1-x}Tb_x multilayered structures, where Tb doping is used to increase the spin relaxation in Fe₅₀Co₅₀ (spin-sink layer). Our key results suggest a programmable modulation of the Gilbert damping of Py, via the parallel (P) and antiparallel (AP) magnetic configurations of Py and Fe-Co-Tb layers, in which the dynamic interlayer coupling plays a highly crucial role.

II. EXPERIMENTS

The main structure of our sample consists of Py(10)/Cu(*t*)/(Fe₅₀Co₅₀)_{1-x}Tb_x(30) (all thicknesses in nm), as schematically depicted in Fig. 1(c). Py is chosen as the response layer for its excellent soft magnetic properties and high saturation magnetization (M_s), while (Fe₅₀Co₅₀)_{1-x}Tb_x acts as a spin-sink layer, the M_s , coercivity (H_c), and spin-scattering effect of which can be controlled by the Tb content, x [12,18]. To determine the optimized Tb content, x , in the heterostructure, a series of (Fe₅₀Co₅₀)_{1-x}Tb_x single layers with various Tb contents are prepared and characterized, as elaborated in later paragraphs. Cu spacers with thicknesses, t , ranging from 1 to 6 nm, are utilized to tune the interlayer coupling between Py and Fe-Co-Tb. It is worth noting that, during the precession of magnetic layers, spin current can transport through Cu due to its weak SOC and long spin-diffusion length [19]. For the thick Cu regime, any Ruderman-Kittel-Kasuya-Yosida [20], pinhole [21], and magnetostatic [22] interactions between Py and Fe-Co-Tb are expected to be suppressed, but dynamic interlayer coupling can still exist. In this case, both P and AP states of the two FM layers can be steadily achieved. For comparison, bilayer samples of Py(10)/Cu(*t*) are prepared as well.

The samples described above are deposited on silicon dioxide (Si/SiO₂) substrates by magnetron sputtering under a base pressure of 1.0×10^{-7} Torr. The Tb concentration in (Fe₅₀Co₅₀)_{1-x}Tb_x is determined and

quantified by energy-dispersive x-ray spectroscopy (EDX). Static and dynamic magnetic properties of the samples are detected by using a vibrating sampling magnetometer (VSM) and the vector network analyzer ferromagnetic resonance (VNA FMR) [7], respectively. During VNA FMR measurements, the samples are subjected to a microwave field, h , with a power of -10 dBm, and an external magnetic field, H , is applied perpendicular to h . Details of the VNA FMR measurements are presented in Appendix A. Later, the multilayer film is further fabricated into a microdevice, and the dynamic behavior of the device is measured by spin-torque FMR (ST FMR) [23]. All measurements are carried out at room temperature.

III. RESULTS AND DISCUSSION

In-plane hysteresis loops of (Fe₅₀Co₅₀)_{1-x}Tb_x single layers are shown in Fig. 1(a), and the corresponding M_s and H_c are listed in Fig. 1(b). With increasing Tb content x , M_s of the (Fe₅₀Co₅₀)_{1-x}Tb_x film is monotonically reduced, originating from the antiferromagnetic coupling between Tb and transition metals [12,24]. For $x = 14$ at. %, an out-of-plane loop is observed in the inset of Fig. 1(a), indicative of a slightly oblique magnetic moment in Fe-Co-Tb along the out-of-plane direction. We find that Fe-Co-Tb films with $x > 14$ at. % are undesirable for the present investigation, due to the further enhanced out-of-plane magnetic anisotropy. Such an enhanced out-of-plane anisotropy is induced by local chemical ordering, giving rise to domains with alternating “up” and “down” magnetization [25]. Therefore, to achieve a large scattering of spin current, while maintaining the in-plane magnetic anisotropy of Fe-Co-Tb, $x = 14$ at. % is chosen for the spin-sink layer. The main magnetic structure in this study then takes the form of Py/Cu(*t*)/(Fe₅₀Co₅₀)₈₆Tb₁₄.

Figure 1(d) reveals the in-plane VSM loops associated with the Py/Cu(*t*)/(Fe₅₀Co₅₀)₈₆Tb₁₄ structure. For $t = 1$ and 2 nm, the coercive field of Py ($H_{c,Py}$) in Py/Cu(*t*)/(Fe₅₀Co₅₀)₈₆Tb₁₄ is about 50 Oe, larger than that in the Py single layer (see Appendix B). This suggests a static interlayer-exchange coupling between Py and Fe-Co-Tb. In contrast, the static interlayer coupling becomes negligible when $t \geq 3$ nm. In this case, two-step switching behavior can be observed, and $H_{c,Py}$ is similar to that of the Py single layer.

Figure 2(a) shows the VNA FMR spectra of the Py/Cu/(Fe₅₀Co₅₀)₈₆Tb₁₄ structure and Py/Cu bilayers. It is noted that the resonance intensity of (Fe₅₀Co₅₀)₈₆Tb₁₄ is quite weak compared with Py (see Appendix C), which makes the obtained FMR signal come almost entirely from Py. From the FMR spectra, we find two interesting phenomena. On one hand, when magnetization switching occurs, ferromagnetic resonances of Py/Cu(*t*)/Fe-Co-Tb with $t = 1$ and 2 nm are suppressed. This behavior can be understood from the M - H curves in Fig. 1(d). Due to

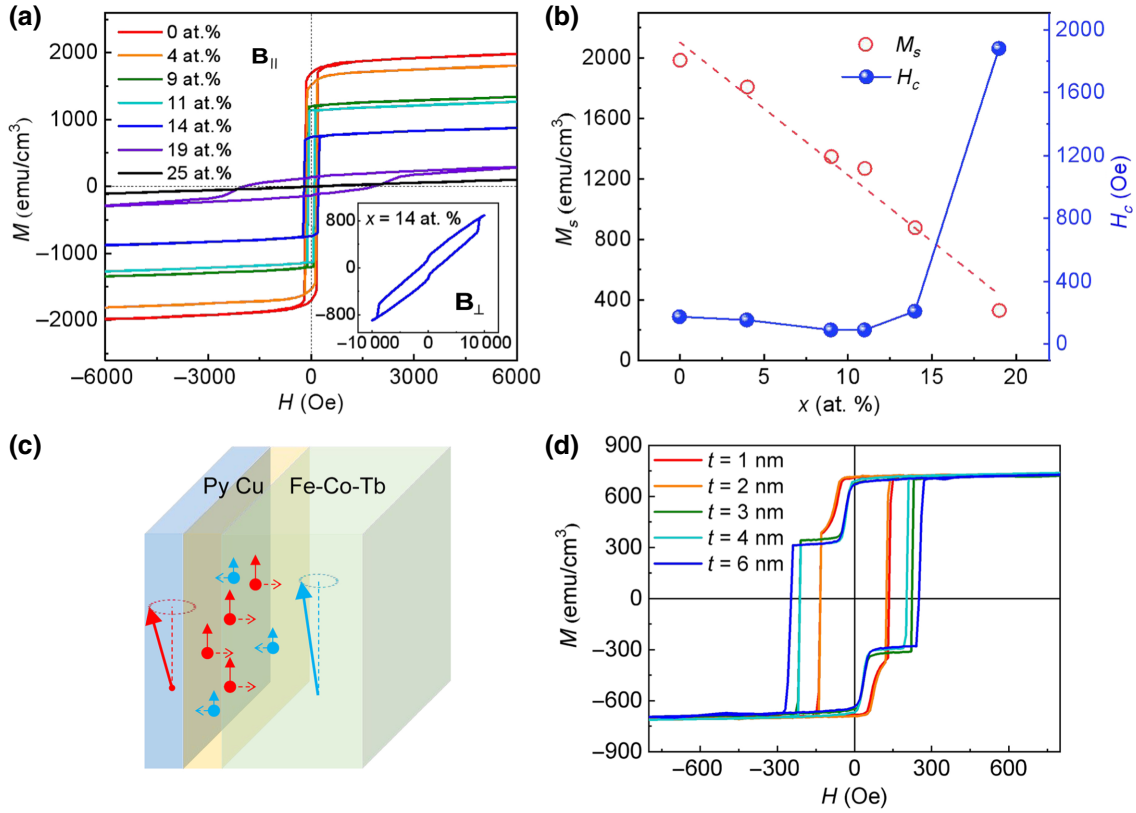


FIG. 1. (a) In-plane hysteresis loops of $(\text{Fe}_{50}\text{Co}_{50})_{1-x}\text{Tb}_x$ single layers with x changing from 0 to 25 at. %. Inset shows the out-of-plane of hysteresis loops of $(\text{Fe}_{50}\text{Co}_{50})_{86}\text{Tb}_{14}$ measured under vertical fields. (b) M_s and H_c of $(\text{Fe}_{50}\text{Co}_{50})_{1-x}\text{Tb}_x$. (c) Schematic structure of Py/Cu/Fe-Co-Tb. (d) In-plane hysteresis loops of Py/Cu(t)/Fe-Co-Tb.

the static interlayer coupling between Py and Fe-Co-Tb, the switching process of Py becomes complex. Therefore, when the applied field is around the coercive field of the Py layer, its magnetization can hardly reach saturation conditions. In this case, no uniform precession of Py can occur. FMR spectra of Py/Cu(1)/Fe-Co-Tb at different frequencies are detailed in Appendix C, and the suppressed resonance is further demonstrated by a frequency response of the microwave transmission signal detected at a fixed magnetic field. On the other hand, for Py/Cu(t)/Fe-Co-Tb with $t \geq 3$ nm, both the resonance field and linewidth of the FMR peak show differences between P and AP states, as will be discussed later. The resonance spectrum can be accurately fit with a sum of symmetrical and antisymmetrical Lorentzian equations. Fitting details are discussed in Appendix C. Figures 2(b) and 2(c) present the frequency-dependent resonance field and linewidth extracted from the FMR spectra, where Py and Fe-Co-Tb are parallel to each other and no switching occurs. Resonance fields of Py/Cu(t)/Fe-Co-Tb with $t \geq 3$ nm are close to that of Py/Cu(t), much larger than the case of $t = 1$ and 2 nm, indicating that the static interlayer coupling between Py and Fe-Co-Tb is dominant when $t \leq 2$ nm and becomes negligible when $t \geq 3$ nm. This result is in line with the

VSM measurements. Kittel's equation provides a quantitative description of the resonance condition for in-plane magnetization [26]:

$$\left(\frac{2\pi f}{\gamma}\right)^2 = H_{\text{eff}}(H_{\text{eff}} + 4\pi M_{\text{eff}}), \quad (1)$$

where γ and $4\pi M_{\text{eff}}$ are the gyromagnetic ratio and effective magnetization of Py, respectively, and H_{eff} is the effective field composed of the Zeeman field and equivalent interlayer-coupling field, H_{IC} . Extracted values of M_{eff} are comparable with the M_s measured by VSM, indicating a negligible surface-perpendicular anisotropy of Py films. Fitting results of H_{IC} for different samples are listed in Table I in Appendix C. H_{IC} for Py/Cu(t)/Fe-Co-Tb decreases from 56.6 to 2.0 Oe when t changes from 1 to 6 nm, and is close to zero when the two FM layers are decoupled.

The frequency-dependent FMR linewidths, ΔH , shown in Fig. 2(c) can be well fitted by $\Delta H = \Delta H_0 + (4\pi\alpha/\gamma)f$ [27], where ΔH_0 denotes inhomogeneous broadening of the film. Exact values of α and ΔH_0 are listed and discussed in Table I in Appendix C. Results show that α in Py/Cu(t)/Fe-Co-Tb increases slightly with t , and the

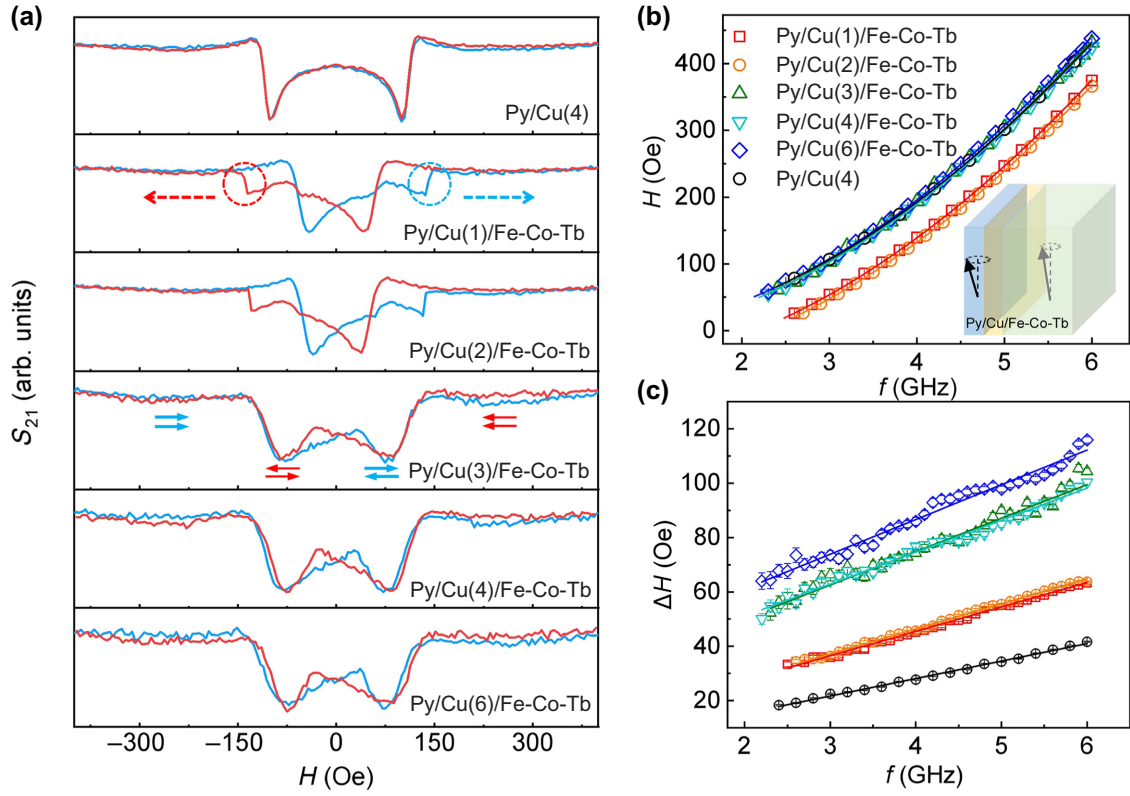


FIG. 2. (a) Typical VNA FMR spectra of Py/Cu(t)/Fe-Co-Tb and Py/Cu(4) measured at 3 GHz. Trace of the scanning magnetic field is represented by the dashed arrow, and magnetic configurations are shown by solid arrows. Suppressed ferromagnetic resonance during the switching process is marked by dashed circles. Frequency dependence of (b) the resonance field and (c) the linewidth extracted from the VNA FMR spectra when Py and Fe-Co-Tb are parallel to each other and no switching occurs.

average value is 0.0154, about 2 times larger than that in Py/Cu(t) (0.0091). We attribute the enhancement of α to dynamic interlayer coupling between Py and Fe-Co-Tb, by which Fe-Co-Tb opens an additional relaxation channel for the magnetization dynamics of Py [28].

We next focus on the configuration-dependent magnetic dynamics by comparing the ferromagnetic resonance of Py/Cu(t)/Fe-Co-Tb with $t \geq 3$ nm in the P and AP states. Figure 3(a) presents the FMR spectra of Py/Cu(6)/Fe-Co-Tb at different microwave frequencies, and corresponding magnetic configurations at different magnetic field regions are marked with arrows. Compared with the P state, both the resonance field and linewidth are smaller when the resonance peak is located in the AP state, and their

extracted values are shown in Figs. 3(b) and 4(a), respectively. In Fig. 3(b), the frequency-dependent resonance field of the P and AP states are separately fitted with Eq. (1), as denoted by the green and orange lines. Interestingly, the fitting result of H_{IC} in the AP state is 16.9 Oe, which is much larger than the value achieved for the P state (2.4 Oe), suggesting a larger interlayer effect for the AP state than the P state. We note that such a configuration-dependent resonance field is neither observed in the Co/Cu/Py structure studied by Salikhov *et al.* [15] nor in Py/Co/Cu/Co/Mn-Ir investigated by Joyeux *et al.* [17]. In the Co₂MnGe/V/Py structure, Salikhov *et al.* [16] reported that the precession frequency of Py in the AP state was smaller than that in the P state, which they interpreted

TABLE I. Extracted parameters of different samples (measured in the P state).

	H_{IC} (Oe)	ΔH_0 (Oe)	α ($\times 10^{-2}$)
Py/Cu(4)	0	2.38 ± 0.42	0.90 ± 0.0003
Py/Cu(1)/Fe-Co-Tb	51.42 ± 0.14	9.52 ± 0.46	1.26 ± 0.0003
Py/Cu(2)/Fe-Co-Tb	56.54 ± 0.16	9.55 ± 0.39	1.29 ± 0.0002
Py/Cu(3)/Fe-Co-Tb	5.27 ± 0.96	25.61 ± 1.93	1.72 ± 0.0011
Py/Cu(4)/Fe-Co-Tb	5.20 ± 0.64	27.55 ± 1.21	1.65 ± 0.0007
Py/Cu(6)/Fe-Co-Tb	2.03 ± 0.51	35.54 ± 1.69	1.79 ± 0.0010

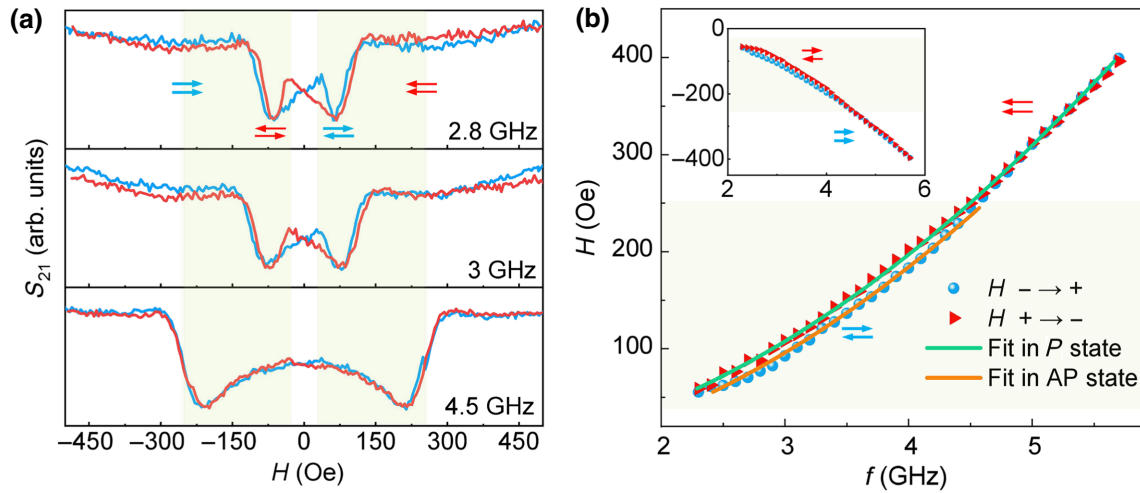


FIG. 3 (a) VNA FMR spectra of Py/Cu(6)/Fe-Co-Tb at different microwave frequencies. Arrows denote the magnetic configuration in different magnetic field regions. (b) Corresponding resonance fields at different frequencies. Blue dots are detected when H scans from negative to positive, while red triangles are detected when H scans in the opposite way. Green and orange lines represent the fitting results in the P and AP states.

as resulting from domain-wall (DW) coupling between two magnetic layers [29]. However, if DW coupling takes effect, in the AP state, the magnetic domains in the Fe-Co-Tb layer would be arranged in a manner that their stray fields are mostly aligned opposite to the direction of Py, which will reduce the external magnetic field in the Py layer. As a result, a higher external field is needed to fulfill the condition of ferromagnetic resonance at a fixed frequency, which, however, is contrary to what we have observed here. We speculate that the enhancement of H_{IC} in the AP state originates from the fieldlike spin torque induced in the Fe-Co-Tb layer [30], as evidenced by some previous pioneering works. For instance, it is predicted [31] and experimentally proved [32] that the

anomalous Hall effect and anisotropic magnetoresistance (AMR) in a ferromagnetic film can be used to generate spin-orbit torques in a similar manner to the spin Hall effect. Additionally, a large fieldlike spin torque can exist in a FM/NM/FM multilayer with extremely low static exchange coupling, just like our present structure [30].

We further study damping control by investigating the configuration-dependent linewidth of Py/Cu/Fe-Co-Tb. As shown in Fig. 4(a), at low frequencies, when the resonance peak is located in the AP state, the linewidth of Py is smaller than that in the P state but increases rapidly with increasing frequency. We suspect that the reduced linewidth during switching between P and AP states may arise from field-driven magnetization reversal.

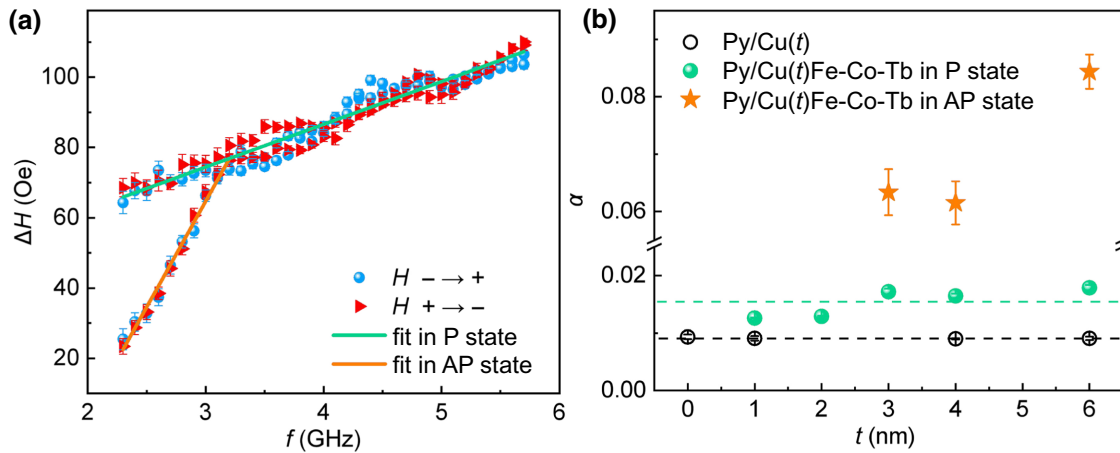


FIG. 4 (a) Frequency dependence of the linewidth of Py/Cu(6)/Fe-Co-Tb. Blue dots are detected when H scans from negative to positive, and red triangles are detected when H scans in the opposite way. Green and orange lines represent the fitting results in the P and AP states, respectively. (b) Gilbert-damping constant of Py/Cu(t) and Py/Cu(t)/Fe-Co-Tb films.

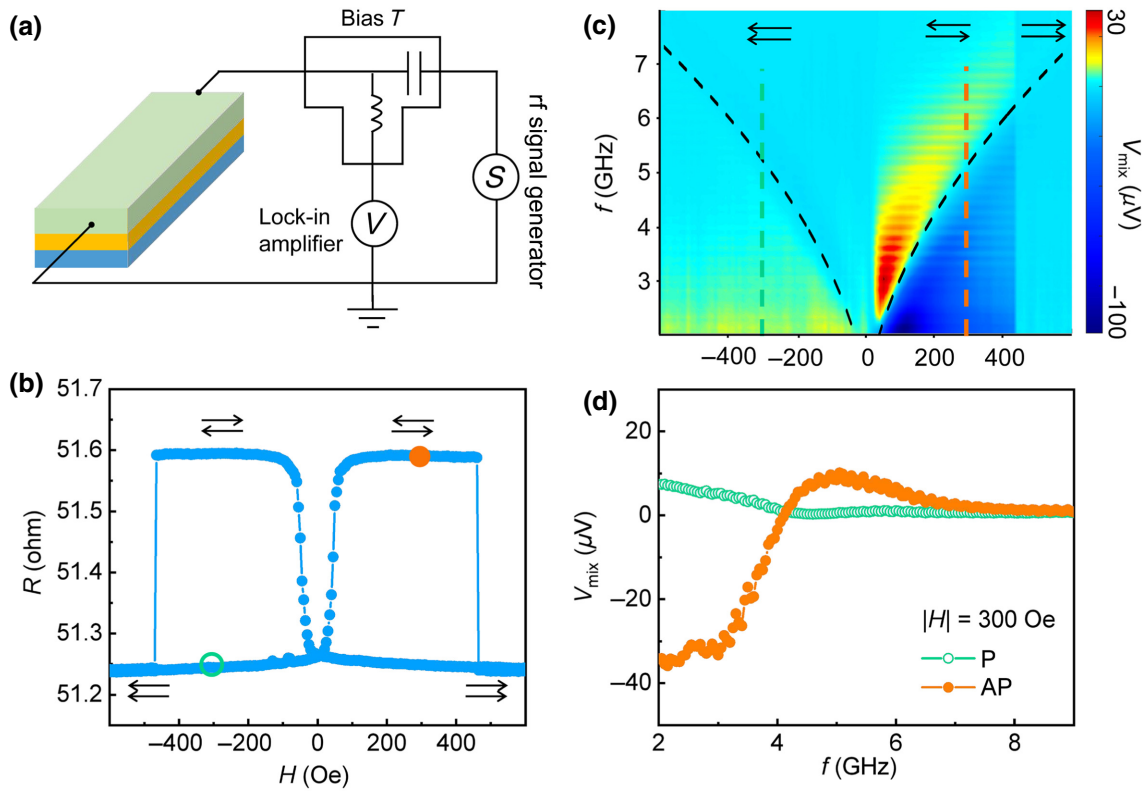


FIG. 5. (a) Schematic structure of the Py/Cu/Fe-Co-Tb device and the circuit used for ST FMR measurements. (b) Magnetoresistance of the device. (c) ST FMR results measured at different frequencies and fields. (d) Typical ST FMR spectra for different magnetic configurations. Green circles are measured in the P state, and red dots are detected in the AP state [corresponding to the circles in (b) and dashed lines in (c)].

During the reversal process, collective motions of magnetic moments are complicated, leading to weakened microwave absorption. This process is determined by the competition between the external field and internal fields, which is frequency independent. Therefore, we can still extract the value of Gilbert damping from the frequency dependency of the linewidth. By fitting the frequency-dependent linewidth in the AP state, the Gilbert damping of Py is extracted as 0.0870, which is about 5 times larger than the value obtained in the P state (0.0178) and about 10 times larger than the average value of Py/Cu(t). Similar results are also observed in Py/Cu(3)/Fe-Co-Tb and Py/Cu(4)/Fe-Co-Tb, and corresponding values of α are summarized in Fig. 4(b). Such an enhancement of α in the AP state is higher than most of the experimental results observed for other methods. For example, the multiple of damping enhancement is usually <2 times for an electrical-field effect [8,33,34], <5 times for a spin-pumping method [35–38] or a spin-orbit-torque method [9,39]. Even for an impurity-doping method, 10 times enhancement of damping is also difficult to implement [7,12,40]. Since the magnetic configuration depends on the external field, α of Py becomes switchable between high and low values, and the switching ratio is 3–5. Such

a switchable Gilbert damping was also indicated in studies performed by Salikhov *et al.* [15,16] and Joyeux *et al.* [17], which can be understood within the model of spin-pumping-induced dynamic interlayer coupling [17]. In the Py/Cu/Fe-Co-Tb structure, the precessing magnetizations of the two magnetic layers interact with each other through the spacer by exchanging nonequilibrium spin currents. When the Py and Fe-Co-Tb magnetizations are parallel, two counterpropagating spin currents with the same polarization direction are pumped into the Cu layer, thus leading to partial cancellation of the spin vector that damps magnetization motion. In contrast, for the AP configuration, the dynamic magnetization of the two layers rotates in the opposite way, such that the spin currents emitted from the magnetic layers carry opposite-spin orientations. In this case, the total spin vector varies over time and never cancels. This then results in a strong dynamic coupling between the two magnetic layers, with an additional damping of precessional motion. It is noted that the fitting result in Fig. 4(a) gives a negative ΔH_0 for the AP state, which may also be associated with the reduced FMR linewidth induced by the switching of Fe-Co-Tb. Since the reduced linewidth is determined by the competition between the external field and internal fields,

it is frequency independent and is most likely embodied in the reduction of ΔH_0 , which might cause an inaccurate estimate of inhomogeneous broadening. During the actual measurement, a negative linewidth can never be observed. The negative ΔH_0 is just a virtual physical quantity arising from extrapolation (see Appendix C).

To verify programmable Gilbert damping in magnonic applications, we further fabricate microstrips ($40 \times 10 \mu\text{m}^2$) from our Py/Cu(6)/Fe-Co-Tb trilayers and characterize their dynamic behavior by ST FMR [Fig. 5(a)]. The measurement is performed with a magnetic field applied in the film plane and 45° to the long axis of the strip. The magnetoresistance of the device is shown in Fig. 5(b), from which one observes steady P and AP states. We first perform field-scanning ST FMR, as shown in Appendix D. The detected rectified voltage proves the effect of spin torque in this structure, which may be the microscopic origin of dynamic interlayer coupling. However, it is found that the intensity of the detected signal changes a lot during the switching process, due to the variation of magnetoresistance and the impedance of the device. This parasitic effect makes it difficult to extract the exact value of the linewidth. Alternatively, here, we perform frequency-scanning ST FMR, and the results are shown in Figs. 5(c) and 5(d). The expected FMR frequencies under different magnetic fields are marked by black dashed lines in Fig. 5(c), which agree well with the rectified signal detected by ST FMR, demonstrating that the rectified signal is caused by the FMR. We find it interesting that both the frequency linewidth and the rectified voltage are controllably switchable between the P and AP states. Commonly, the measured FMR frequency linewidth is the sum of extrinsic inhomogeneous line broadening and the Gilbert-damping contribution. As discussed in detail in Appendix D, the calculated Gilbert damping in the AP state is more than 3 times larger than that in the P state. Such a magnetic-configuration-dependent dynamic damping achieved by ST FMR is consistent with the results obtained from the VNA FMR, which can be utilized for reconfigurable magnonic devices [5], and provides opportunities for broadband microwave detection [41].

IV. CONCLUSION

We exploit an effective strategy to tune the dynamic behavior and Gilbert damping of Py thin films, by capping with Cu/Fe-Co-Tb layers with adjustable interlayer coupling and magnetic configurations. Frequency-dependent FMR measurements demonstrate that the Gilbert-damping constant of Py/Cu/Fe-Co-Tb is enhanced up to 0.0870 when Py and Fe-Co-Tb are antiparallel to each other; this value is about 5 times larger than the case in which the two magnetic layers are parallel, and 10 times larger than that of Py/Cu. By changing the thickness of the Cu spacer, we systematically study the interlayer coupling between

Py and Fe-Co-Tb. It is demonstrated that dynamic interlayer coupling between ferromagnetic layers plays a key role in increased damping. By ST FMR, we reveal that such configuration-dependent dynamic behavior remains intact in nano- and microdevices. Our studies might provide important information for future magnonic devices toward logic and high-speed computing.

ACKNOWLEDGMENTS

This work is supported by the National Key Research and Development Program of China (Grant No. 2017YFA0204800) and the National Natural Science Foundation of China (Grants No. 52071079, No. 51971109, No. 51771053, No. 51732010, and No. 11974379). W.Z. and P.K.J.W. are supported by the Fundamental Research Funds for the Central Universities. P.K.J.W. acknowledges financial support from the Natural Science Foundation of Shaanxi Province, China (Grant No. 2021JM-042).

APPENDIX A: DETAILS OF THE VNA FMR MEASUREMENT

The VNA FMR measurements are performed with a vector network analyzer (Keysight model N5234A). As shown in Fig. 6, during the measurement, the film is placed face down on a coplanar waveguide (CPW) and subjected to a microwave field, h , with the power of -10 dBm (inset of Fig. 1). An in-plane magnetic field, H , is applied perpendicular to h and swept between -800 and $+800$ Oe. The process in which H scans from -800 to 800 Oe is denoted by $L1$, and H scanning from 800 to -800 Oe is denoted by $L2$. Time-varying magnetic fields produced by the sample under FMR excitation will inductively couple in the CPW, altering the total inductance of the microwave

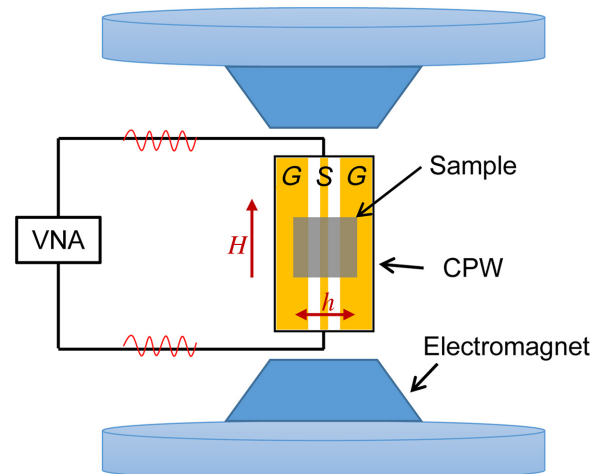


FIG. 6. Schematic diagram of the VNA FMR measurement setup.

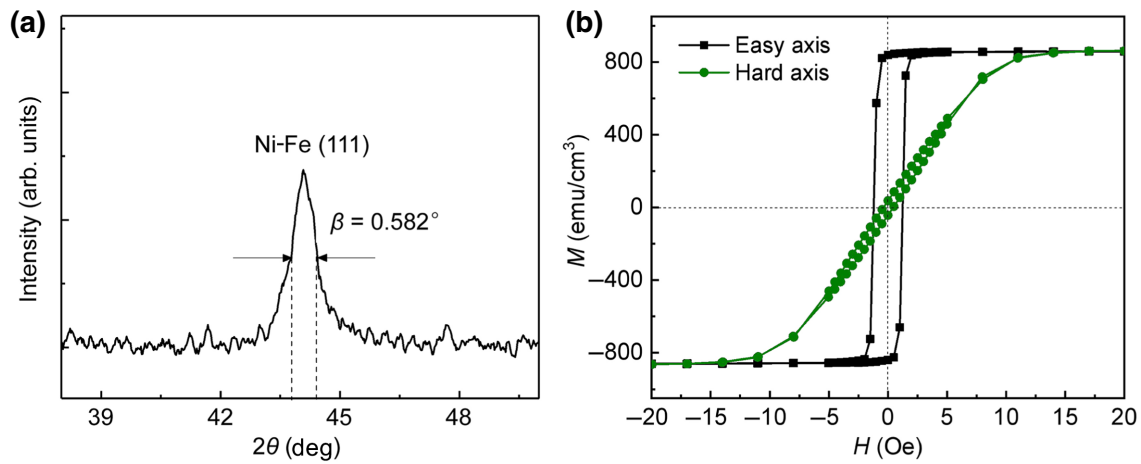


FIG. 7. (a) X-ray diffraction pattern and (b) in-plane hysteresis loops of Py film with a thickness of 10 nm.

circuit. The microwave absorption is at a maximum when the FMR condition is met, then a reduced transmission signal (S_{21}) is detected by the VNA. As described in the main text, field-swept FMR spectra are obtained by measuring S_{21} at a fixed frequency. To achieve the uniform precession of Py, the frequency of the microwave changes from 2.3 to 6.0 GHz according to Kittel's equation [26]. All measurements are carried out at room temperature.

APPENDIX B: STRUCTURE AND MAGNETIC PROPERTIES OF THE Py SINGLE-LAYER FILM

Structure and magnetic properties of the Py single-layer film are characterized by x-ray diffraction (XRD) and a VSM, respectively. Figure 7(a) is the XRD pattern of the Py film, from which the diffraction peak of the Ni – Fe(111) texture is clearly observed. According to

the well-known Debye-Scherrer formula, the average grain size of Py is calculated to be 15 nm. In-plane hysteresis loops of Py single layers are shown in Fig. 7(b). The coercive field of the Py film is about 2 Oe, and the saturation magnetization is about 865.5 emu/cm^3 .

APPENDIX C: DETAILED ANALYSIS OF THE RESONANCE SPECTRA DETECTED BY VNA FMR

The VNA FMR spectra of the $(\text{Fe}_{50}\text{Co}_{50})_{1-x}\text{Tb}_x$ single layer are shown in Fig. 8. With the increased Tb content, the resonance intensity of Fe-Co-Tb is attenuated, which becomes almost invisible for $x = 4 \text{ at. } \%$. Since the resonance signal is much weaker compared with Py, we regard that the observed FMR signal in our study comes almost entirely from Py.

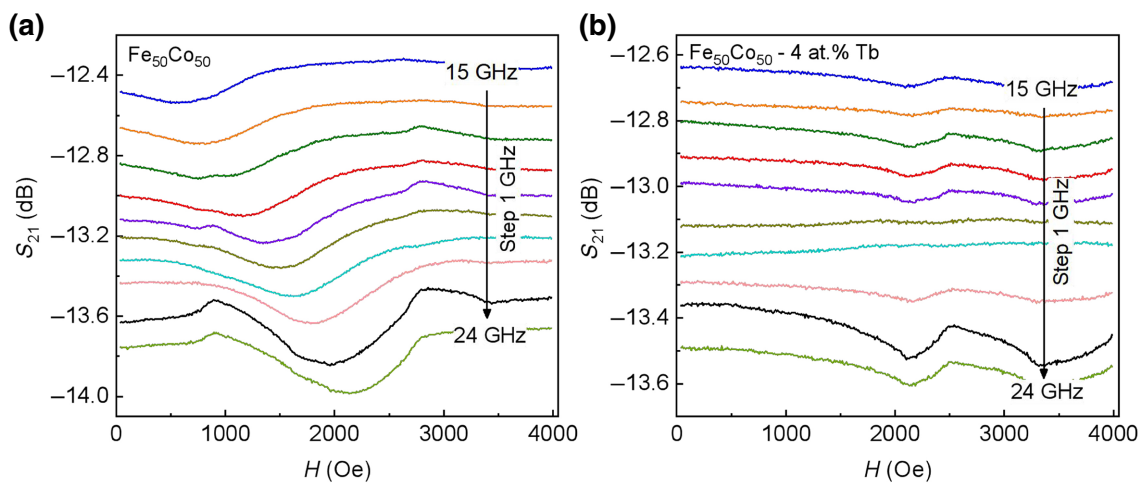


FIG. 8. Typical FMR spectra of (a) $\text{Fe}_{50}\text{Co}_{50}$ and (b) $(\text{FeCo})_{96}\text{Tb}_4$. Due to the large natural resonance field and linewidth of Co, spectra in the lower-frequency region are almost invisible. With increasing Tb concentration in Fe-Co-Tb, the intensity of microwave absorption is further reduced.

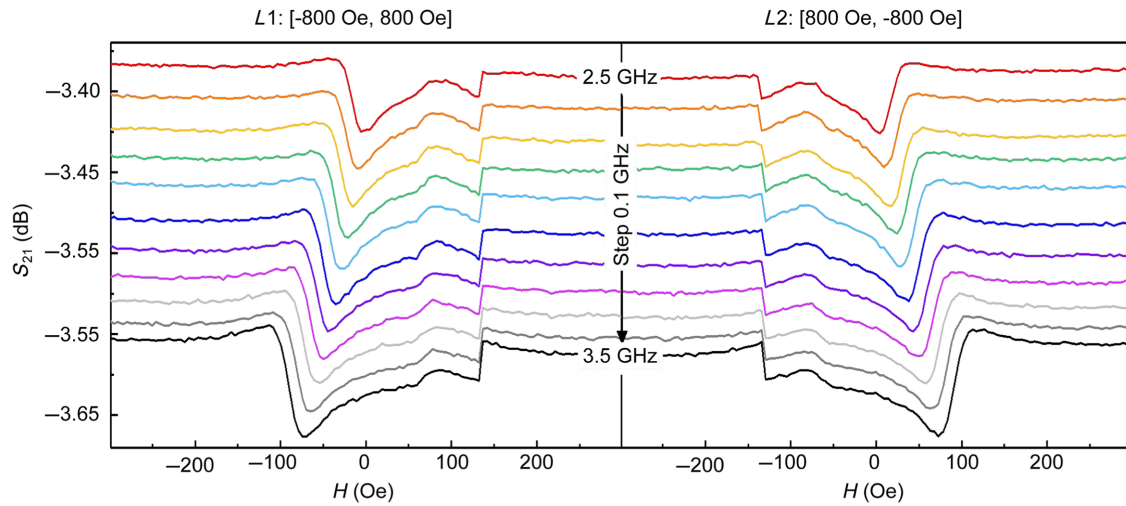


FIG. 9. Full FMR spectra of Py/Cu(1)/(FeCo)₈₆Tb₁₄ at different frequencies. *L1* means *H* scans from -800 to 800 Oe, and *L2* means *H* scans from 800 to -800 Oe.

Figure 9 presents the full resonance spectra of Py/Cu(1)/Fe-Co-Tb (including *L1* and *L2*) detected by VNA FMR at different frequencies. When magnetization switching occurs (in the positive-field region of *L1* and negative-field region of *L2*), the FMR peak of Py/Cu/Fe-Co-Tb is suppressed due to interlayer coupling, which is almost independent of the microwave frequency.

To further demonstrate the suppressed resonance in Py/Cu/Fe-Co-Tb with large interlayer coupling, a frequency response of the microwave-transmission signal is detected at a fixed magnetic field. As shown in Fig. 10, when the magnetic field scans from positive to negative, the switching of Py in Py/Cu/Fe-Co-Tb with a thin

Cu spacer takes place at around -120 Oe. In this case, the resonance peak at -120 Oe disappears; this can be clearly seen in Fig. 10, in comparison with the case of $H = 120$ Oe.

The resonance spectrum can be accurately fitted with the sum of symmetrical and antisymmetrical Lorentzian equations [7]:

$$|S_{21}| = \frac{K_1 \Delta H^2 + K_2 \Delta H (H - H_{\text{FMR}})}{\Delta H^2 + 4(H - H_{\text{FMR}})^2},$$

where H_{FMR} and ΔH are the resonance field and linewidth (full width at half maximum) of the resonance peak. K_1 and K_2 are coefficients of the symmetrical Lorentzian and antisymmetrical Lorentzian functions, respectively. Figure 11 shows the fitting results of the FMR spectra at different frequencies in the P and AP states. It is also important to notice that, in our study, the frequency range we use starts from 2.3 GHz, corresponding to a resonance field of about 60 Oe, which is close to the lower boundary of the steady AP state. If the frequency is further reduced, the resonance field of Py given by Kittel's equation is not sufficient to make its magnetization orientate strictly antiparallel to Fe-Co-Tb. In another word, Kittel's equation does not work at lower frequencies. In this case, the magnetic moment of Py is not in a uniform precession but a complex spin-wave resonance. Therefore, the detected linewidth of the FMR response at lower frequencies should be larger than that extrapolated from the uniform precession model, by which the linear variation of the linewidth is broken down. To ensure the accuracy of Gilbert damping, we focus on analyzing the linear variation of the frequency-dependent linewidth.

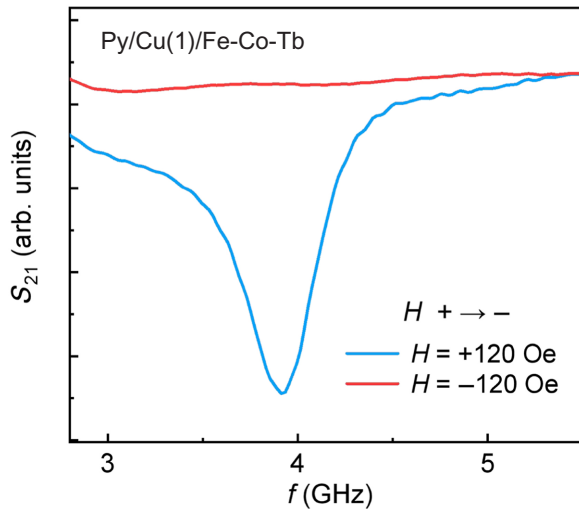


FIG. 10. Frequency response of the microwave transmission signal for Py/Cu(1)/Fe-Co-Tb detected at 120 and -120 Oe. Magnetic field changes from positive to negative, resulting in a complex switching process of Py around -120 Oe.

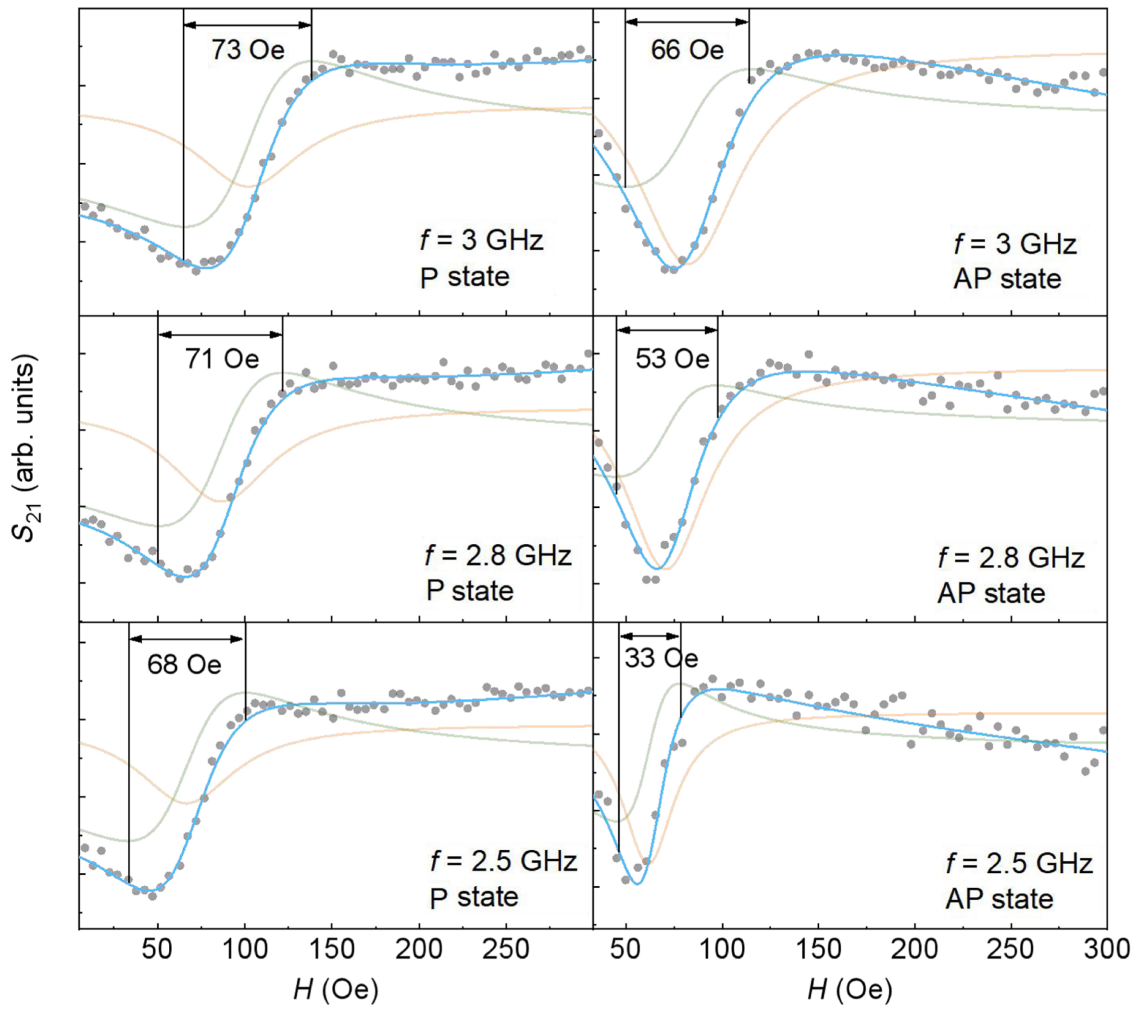


FIG. 11. Fitting results of the FMR spectra at different frequencies in the P and AP states. Gray dots are experimental data. Blue lines represent the fitting results of the full FMR spectra. Orange and green lines denote symmetric and antisymmetric resonance components, respectively. Linewidth (full width at half maximum) of the FMR spectra at different frequencies are marked in the corresponding figures.

Table I lists the extracted parameters (the equivalent interlayer coupling field, H_{IC} ; the inhomogeneous broadening, ΔH_0 ; and the Gilbert damping, α) of Py/Cu(4) and Py/Cu(t)/Fe-Co-Tb. With increasing Cu thickness, ΔH_0 monotonously increases from 9.52 Oe ($t = 1$ nm) to 35.53 Oe ($t = 6$ nm); these values are much larger than the value of Py/Cu(4) (2.38 Oe). This may be attributed to the increased inhomogeneity of the film. A similar phenomenon was reported previously in a Cu/Fe-Co-Gd/Cu multilayer film by Zhang *et al.* [42]. In their study, the interface roughness between the Cu seed layer and Fe-Co-Gd layer is enhanced with the increased thickness of the Cu seed layer, which leads to an increase of the roughness and grain size at the surface of the Fe-Co-Gd layer. The situation is similar here for Py/Cu/Fe-Co-Tb structures. The induced interface roughness may increase

the inhomogeneity of the film, thus leading to a large ΔH_0 in Py/Cu/Fe-Co-Tb films.

APPENDIX D: DETAILS OF THE ST FMR MEASUREMENT

Figure 12 presents the resonance spectra detected by field-scanning ST FMR. The signal intensity detected by ST FMR changes obviously before and after the magnetic switching process, which is different from the VNA FMR spectra. This difference can be explained by the working principles of the two measurement techniques. In conventional ST FMR, the ferromagnetic resonance is induced through current-induced torque acting on magnetization. The strength of the spin torque is determined by the input power of the signal source and the

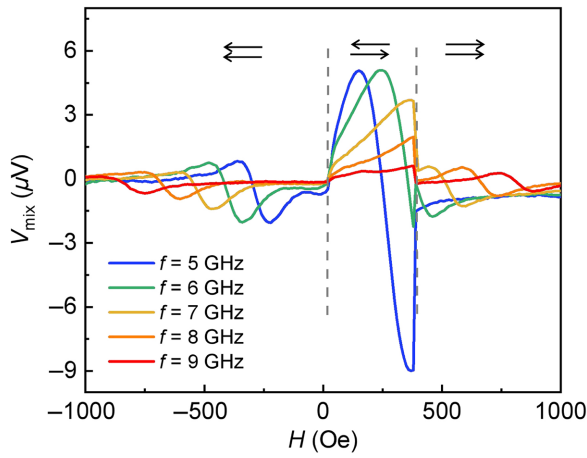


FIG. 12. Field-scanning ST FMR spectra of the Py/Cu(6)/Fe-Co-Tb microdevice at different frequencies. Magnetic configurations in different field regions are illustrated by arrows.

impedance of the device. Magnetic resonance can be detected via a rectified longitudinal dc voltage caused by mixing of the microwave current with resistance

oscillations produced by the precessing magnet via AMR or spin Hall magnetoresistance. Therefore, the intensity of the detected signal changes a lot, since the magnetoresistance and impedance of the device become different during the switching process. For the VNA FMR measurement, a microwave field is applied to the film through a CPW. The microwave absorption is at a maximum when the FMR condition is met, then a reduced transmission signal can be detected by the VNA. Since the resistance of the sample has little influence on the microwave absorption intensity, the signal intensity detected by VNA FMR does not change dramatically in different magnetic states.

The measured FMR frequency linewidth is the sum of extrinsic inhomogeneous line broadening and the Gilbert-damping contribution, Δf_{Gil} . The latter is related to the Gilbert-damping parameter by

$$\Delta f_{Gil} = \alpha\gamma(2H + 4\pi M_{eff}),$$

where γ and M_{eff} are the gyromagnetic ratio and effective magnetization of Py, respectively. In our study, frequency-scanning FMR spectra in the P and AP states [data are from Fig. 5(c)] are shown in Figs. 13(a) and

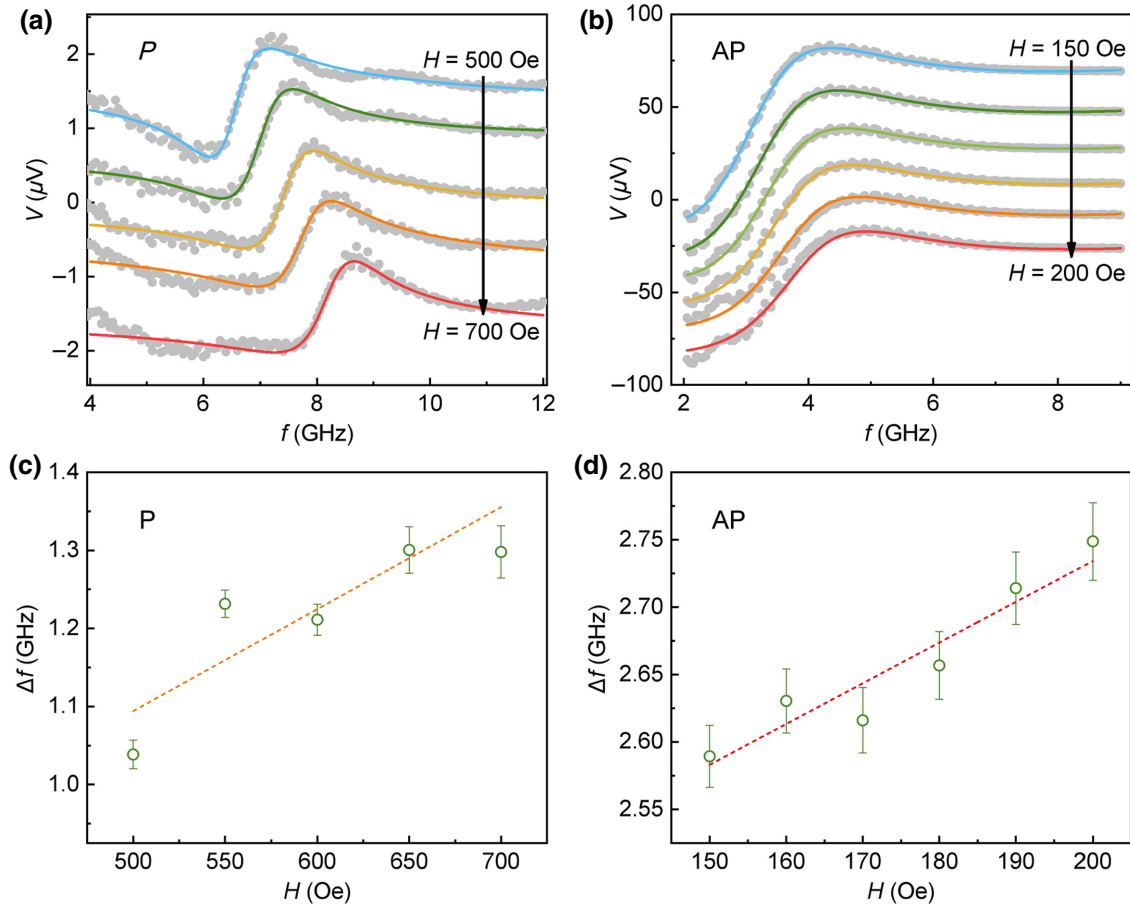


FIG. 13. Frequency-scanning FMR spectrum detected by ST FMR in the (a) P and (b) AP states. Corresponding field-dependent linewidths in the (c) P and (d) AP states.

13(b), and corresponding field-dependent linewidths are shown in Figs. 13(c) and 13(d), respectively. As a common problem for frequency-scanning measurements, the ST FMR spectrum is dominated by frequency-dependent nonmagnetic background signals caused by nonlinearities and impedance mismatches within the microwave circuit [43]. Therefore, the value of Gilbert damping is hard to accurately extract. Here, we roughly calculate the ratio between α in the P and AP states by comparing the slope of $\Delta f_{\text{Gil}} - H$ curves. Results show that Gilbert damping in the AP state is more than 3 times larger than that in the P state. Considering the difference between the microscale device and the continuous film, as well as the background disturbance in the frequency-scanning spectrum, we conclude that such a magnetic-configuration-dependent dynamic damping achieved by ST FMR is almost consistent with the results obtained from the VNA FMR.

-
- [1] S. Neusser and D. Grundler, Magnonics: Spin waves on the nanoscale, *Adv. Mater.* **21**, 2927 (2009).
- [2] J. Han, P. Zhang, J. T. Hou, S. A. Siddiqui, and L. Liu, Mutual control of coherent spin waves and magnetic domain walls in a magnonic device, *Science* **366**, 1121 (2019).
- [3] H. Qin, R. B. Hollander, L. Flajsman, F. Hermann, R. Dreyer, G. Woltersdorf, and S. Van Dijken, Nanoscale magnonic fabry-pérot resonator for Low-loss spin-wave manipulation, *Nat. Commun.* **12**, 2293 (2021).
- [4] M. C. Hickey and J. S. Moodera, Origin of Intrinsic Gilbert Damping, *Phys. Rev. Lett.* **102**, 137601 (2009).
- [5] H. Wang, M. Madami, J. Chen, L. Sheng, M. Zhao, Y. Zhang, W. He, C. Guo, H. Jia, S. Liu, Q. Song, X. Han, D. Yu, G. Gubbiotti, and H. Yu, Tunable damping in magnetic nanowires induced by chiral pumping of spin waves, *ACS Nano* **15**, 9076 (2021).
- [6] D. Grundler, Reconfigurable magnonics heats up, *Nat. Phys.* **11**, 438 (2015).
- [7] Y. Yin, F. Pan, M. Ahlberg, M. Ranjbar, P. Dürrenfeld, A. Houshang, M. Haidar, L. Bergqvist, Y. Zhai, R. K. Dumas, A. Delin, and J. Åkerman, Tunable permalloy-based films for magnonic devices, *Phys. Rev. B* **92**, 024427 (2015).
- [8] H. Fulara, M. Zahedinejad, R. Khymyn, M. Dvornik, S. Fukami, S. Kanai, H. Ohno, and J. Åkerman, Giant voltage-controlled modulation of spin Hall nano-oscillator damping, *Nat. Commun.* **11**, 4006 (2020).
- [9] J. Holanda, H. Saglam, V. Karakas, Z. Zang, Y. Li, R. Divan, Y. Liu, O. Ozatay, V. Novosad, J. E. Pearson, and A. Hoffmann, Magnetic Damping Modulation in $\text{IrMn}_3/\text{Ni}_{80}\text{Fe}_{20}$ via the Magnetic Spin Hall effect, *Phys. Rev. Lett.* **124**, 087204 (2020).
- [10] Y. Tserkovnyak, A. Brataas, and G. E. W. Bauer, Spin Pumping and Magnetization Dynamics in Metallic Multilayers, *Phys. Rev. B* **66**, 224403 (2002).
- [11] Y. Tserkovnyak, A. Brataas, and G. E. W. Bauer, Enhanced gilbert damping in thin ferromagnetic films, *Phys. Rev. Lett.* **88**, 117601 (2002).
- [12] Q. Chen, Y. Yin, H. Yuan, X. Zhou, Z. Huang, J. Du, and Y. Zhai, Effect of dilute rare-earth doping on magnetodynamic properties of permalloy films, *IEEE Magn. Lett.* **10**, 5501705 (2019).
- [13] B. Heinrich, Y. Tserkovnyak, G. Woltersdorf, A. Brataas, R. Urban, and G. E. W. Bauer, Dynamic Exchange Coupling in Magnetic Bilayers, *Phys. Rev. Lett.* **90**, 187601 (2003).
- [14] A. A. Baker, A. I. Figueroa, C. J. Love, S. A. Cavill, T. Hesjedal, and G. Van Der Laan, Anisotropic Absorption of Pure Spin Currents, *Phys. Rev. Lett.* **116**, 047201 (2016).
- [15] R. Salikhov, R. Abrudan, F. Brüssing, St. Buschhorn, M. Ewerlin, D. Mishra, F. Radu, I. A. Garifullin, and H. Zabel, Precessional dynamics and damping in Co/Cu/Py spin valves, *Appl. Phys. Lett.* **99**, 092509 (2011).
- [16] R. Salikhov, R. Abrudan, F. Brüssing, K. Gross, C. Luo, K. Westerholt, and H. Zabel, Configurational dependence of the magnetization dynamics in spin valve systems: Influence of spin pumping and domain wall induced coupling, *Phys. Rev. B* **86**, 144422 (2012).
- [17] X. Joyeux, T. Devolder, J.-V. Kim, Y. Gomez De La Torre, S. Eimer, and C. Chappert, Configuration and temperature dependence of magnetic damping in spin valves, *J. Appl. Phys.* **110**, 063915 (2011).
- [18] M. F. Ruane and J. Calkins, Characterization of amorphous TbFeCo films for magneto-optical media, *J. Appl. Phys.* **63**, 3630 (1988).
- [19] S. Yakata, Y. Ando, T. Miyazaki, and S. Mizukami, Temperature dependences of spin-diffusion lengths of Cu and Ru layers, *Jap. J. Appl. Phys.* **45**, 3892 (2006).
- [20] P. Grünberg, R. Schreiber, Y. Pang, M. B. Brodsky, and H. Sowers, Layered Magnetic Structures: Evidence for Antiferromagnetic Coupling of Fe Layers Across Cr Interlayers, *Phys. Rev. Lett.* **57**, 2442 (1986).
- [21] J. F. Bobo, H. Kikuchi, O. Redon, E. Snoeck, M. Piecuch, and R. L. White, Pinholes in antiferromagnetically coupled multilayers: Effects on hysteresis loops and relation to biquadratic exchange, *Phys. Rev. B* **60**, 4131 (1999).
- [22] U. Rücker, S. Demokritov, E. Tsymlal, P. Grünberg, and W. Zinn, Biquadratic coupling in Fe/Au/Fe trilayers: Experimental evidence for the magnetic-dipole mechanism, *J. Appl. Phys.* **78**, 387 (1995).
- [23] J. Zhu, J. A. Katine, G. E. Rowlands, Y.-J. Chen, Z. Duan, J. G. Alzate, P. Upadhyaya, J. Langer, P. K. Amiri, K. L. Wang, and I. N. Krivorotov, Voltage-induced Ferromagnetic Resonance in Magnetic Tunnel Junctions, *Phys. Rev. Lett.* **108**, 197203 (2012).
- [24] W. Zhang, D. Zhang, P. K. Wong, H. Yuan, S. Jiang, G. Van Der Laan, Y. Zhai, and Z. Lu, Tuning of gilbert damping in spin-valve trilayer by insertion of rare-earth nanolayers, *ACS Appl. Mater. Interfaces* **7**, 17070 (2015).
- [25] M. Hennes, A. Merhe, X. Liu, D. Weder, C. V. K. Schmisling, M. Schneider, C. M. Günther, B. Mahieu, G. Malinowski, M. Hehn, D. Lacour, F. Capotondi, E. Pedersoli, I. P. Nikolov, V. Chardonnet, E. Jal, J. Lüning, and B. Vodungbo, Laser-induced ultrafast demagnetization and perpendicular magnetic anisotropy reduction in a $\text{Co}_{88}\text{Tb}_{12}$ thin film with stripe domains, *Phys. Rev. B* **102**, 174437 (2020).

- [26] C. Kittel, On the theory of ferromagnetic resonance absorption, *Phys. Rev.* **73**, 155 (1948).
- [27] S. S. Kalarickal, P. Krivosik, M. Wu, C. E. Patton, M. L. Schneider, P. Kabos, T. J. Silva, and J. P. Nibarger, Ferromagnetic resonance linewidth in metallic thin films: Comparison of measurement methods, *J. Appl. Phys.* **99**, 093909 (2006).
- [28] R. Urban, G. Woltersdorf, and B. Heinrich, Gilbert Damping in Single and Multilayer Ultrathin Films: Role of Interfaces in Nonlocal Spin Dynamics, *Phys. Rev. Lett.* **87**, 217204 (2001).
- [29] W. S. Lew, S. P. Li, L. Lopez-Diaz, D. C. Hatton, and J. A. C. Bland, Mirror Domain Structures Induced by Interlayer Magnetic Wall Coupling, *Phys. Rev. Lett.* **90**, 217201 (2003).
- [30] C. Abert, H. Sepelri-Amin, F. Bruckner, C. Vogler, M. Hayashi, and D. Suess, Fieldlike and Dampinglike Spin-Transfer Torque in Magnetic Multilayers, *Phys. Rev. Appl.* **7**, 054007 (2017).
- [31] T. Taniguchi, J. Grollier, and M. D. Stiles, Spin-Transfer Torques Generated by the Anomalous Hall Effect and Anisotropic Magnetoresistance, *Phys. Rev. Appl.* **3**, 044001 (2015).
- [32] J. D. Gibbons, D. Macneill, R. A. Buhrman, and D. C. Ralph, Reorientable Spin Direction for Spin Current Produced by the Anomalous Hall Effect, *Phys. Rev. Appl.* **9**, 064033 (2018).
- [33] T. Li, B. Zhang, H. Wang, J. Zhao, K. Wang, and X. Zhang, Piezostain modulation of magnetic damping in MBE-grown epitaxial $\text{Co}_2\text{FeAl}/\text{GaAs}$ heterostructure, *J. Phys. D: Appl. Phys.* **52**, 455001 (2019).
- [34] A. Sakoguchi, D. Oshima, S. Iwata, and T. Kato, Electric-field modulation of perpendicular magnetic anisotropy and damping constant in $\text{MgO}/\text{Co}/\text{Pt}$ trilayers, *IEEE Trans. Magn.* **58**, 4200105 (2022).
- [35] W. Fan, Q. Fu, Q. Qian, Q. Chen, W. Liu, X. Zhou, H. Yuan, J. Yue, Z. Huang, S. Jiang, Z. Kou, and Y. Zhai, Investigation of magnetization dynamics damping in $\text{Ni}_{80}\text{Fe}_{20}/\text{Nd-Cu}$ bilayer at room temperature, *AIP Adv.* **8**, 056325 (2018).
- [36] S. Crossley, A. G. Swartz, K. Nishio, Y. Hikita, and H. Y. Hwang, All-oxide ferromagnetic resonance and spin pumping with SrIrO_3 , *Phys. Rev. B* **100**, 115163 (2019).
- [37] R. Sun, Y. Li, Z. K. Xie, Y. Li, X.-T. Zhao, W. Liu, Z. D. Zhang, T. Zhu, Z.-H. Cheng, and W. He, Determination of spin pumping effect in CoFeB/Ir bilayer, *J. Magn. Magn. Mater.* **497**, 165971 (2020).
- [38] G. Wu, D. Wu, Y. Ren, Q. Y. Jin, and Z. Zhang, Topological surface state manipulation of magnetic damping and surface anisotropy in topological insulator/nonmagnet/ CoFe heterostructures, *Phys. Rev. B* **103**, 014419 (2021).
- [39] S. Kasai, K. Kondou, H. Sukegawa, S. Mitani, K. Tsukagoshi, and Y. Otani, Modulation of effective damping constant using spin Hall effect, *Appl. Phys. Lett.* **104**, 092408 (2014).
- [40] W. Zhang, S. Jiang, P. K. J. Wong, L. Sun, Y. K. Wang, K. Wang, M. P. De Jong, W. G. Van Der Wiel, G. Van Der Laan, and Y. Zhai, Engineering gilbert damping by dilute Gd doping in soft magnetic Fe thin films, *J. Appl. Phys.* **115**, 17A308 (2014).
- [41] L. Zhang, B. Fang, J. Cai, W. Wu, B. Zhang, B. Wang, P. K. Amiri, G. Finocchio, and Z. Zeng, Enhanced broadband radio frequency detection in nanoscale magnetic tunnel junction by interface engineering, *ACS Appl. Mater. Interfaces* **11**, 29382 (2019).
- [42] D. Zhang, S. Jiang, C. Luo, Y. Wang, W. Rui, Y. Zhai, J. Du, and H. Zhai, Influence of the interface on the magnetic properties of ferromagnetic ultrathin films with various adjacent copper thicknesses, *J. Appl. Phys.* **115**, 17C108 (2014).
- [43] A. M. Goncalves, I. Barsukov, Y.-J. Chen, L. Yang, J. A. Katine, and I. N. Krivorotov, Spin torque ferromagnetic resonance with magnetic field modulation, *Appl. Phys. Lett.* **103**, 172406 (2013).